

# Ultra-Compact Microsystems-Based Confocal Endomicroscope

Gaoming Li, Xiyu Duan, Miki Lee, Mayur Birla<sup>ID</sup>, Jing Chen, Kenn R. Oldham<sup>ID</sup>,  
Thomas D. Wang<sup>ID</sup>, *Member, IEEE*, and Haijun Li<sup>ID</sup>

**Abstract**—Point-of-care medical diagnosis demands immediate feedback on tissue pathology. Confocal endomicroscopy can provide real-time in vivo images with histology-like features. The working channel in medical endoscopes are becoming smaller in dimension. Microsystems methods can produce tiny mechanical scanners. We demonstrate a flexible fiber instrument for in vivo imaging as an endoscope accessory. The optical path is folded on-axis to reduce length while allowing the beam to expand and achieve a numerical aperture of 0.41. A high-speed parametric resonance mirror produces large deflection angles  $> 13^\circ$ , and is mounted on a 2 mm diameter chip designed with clamp structures for reduced space. A compact lens assembly provides diffraction-limited lateral and axial resolution of 1.5 and 12  $\mu\text{m}$ , respectively. A working distance of 50  $\mu\text{m}$  and field-of-view of 350  $\mu\text{m} \times 350 \mu\text{m}$  are achieved. Miniature apparatus is fabricated to assemble and align the scanhead components. The optics and scanner are packaged in a distal tip with 2.4 mm diameter and 10 mm rigid length. These dimensions allow the endomicroscope to pass forward easily through the 2.8 mm diameter working channel in medical endoscopes commonly used in clinical practice. Fluorescence images are collected in vivo at 10 frames per second in the colon of genetically-engineered mice that spontaneously develop adenomas. A FITC-labeled peptide heterodimer is administered intravenously to provide specific contrast. Sub-cellular structures are visualized to distinguish pre-malignant from normal mucosa. These

results demonstrate use of microsystems methods to produce an ultra-compact instrument with sufficiently small dimensions for broad use.

**Index Terms**—Optical imaging, endoscopy, system design, molecular and cellular imaging, gastrointestinal tract.

## I. INTRODUCTION

**M**EDICAL endoscopes are inserted into hollow organs found throughout the human body to identify pre-malignant lesions that may progress to cancer and perform therapeutic interventions [1]. Conventional endoscopy with white light illumination has limited ability to distinguish pre-cancerous from benign lesions [2]. The spatial information provided by reflectance images alone is not adequate to distinguish between pre-cancerous and benign lesions, hence a biopsy is necessary. Tissue biopsies are often collected from abnormal appearing sites, such as masses, nodules, and polyps, that have no malignant potential. Frequently, more biopsies are taken than are actually needed [3]. A variety of technologies are being developed for use as an endoscope accessory to perform “optical” biopsy in vivo [4]–[6]. Clinical endoscopes are trending toward a thinner overall dimension, and most working channels are now only 2.8 mm in diameter. Adjunct instruments must have a distal tip with diameter  $< 2.4$  mm and a rigid length  $< 10$  mm to pass forward easily through the large bending angle located at the channel entrance. Confocal endomicroscopes use the core of an optical fiber as a “pinhole” to allow only the light that originates from the plane of focus below the tissue surface to pass while rejecting scattered photons [7]. Images with sub-cellular resolution can be achieved to provide rapid histological assessment and guide tissue biopsy [8], [9]. The optical design, alignment mechanism, and packaging strategy for accessory instruments must meet these demanding size requirements for broad clinical use.

Microsystems technology is a powerful strategy to provide useful function in devices with a small footprint for medical applications [10]. This approach provides great versatility for the design of miniature scanning and actuation mechanisms used in flexible fiber instruments [11]. Tiny devices can be designed to produce large deflection angles at high scan speeds with low power requirements and fast response times. Simple fabrication processes have potential for mass manufacture at low cost [12]. Devices based on electrostatic, electrothermal, piezoelectric, and electromagnetic principles

Manuscript received October 23, 2019; revised January 17, 2020 and January 23, 2020; accepted January 25, 2020. Date of publication February 3, 2020; date of current version June 30, 2020. This work was supported in part by the National Institutes of Health (NIH) under Grant R01 EB020644 (KRO) and in part by the University of Michigan–Beijing Institute of Collaborative Innovation (BICI) Partnership Program (TDW). (Gaoming Li, Xiyu Duan, and Haijun Li contributed equally to this work.) (Corresponding author: Haijun Li.)

Gaoming Li, Miki Lee, Jing Chen, and Haijun Li are with the Division of Gastroenterology, Department of Internal Medicine, University of Michigan, Ann Arbor, MI 48104 USA (e-mail: gaomingl@umich.edu; leemiki@umich.edu; jchenum@med.umich.edu; haijunl@umich.edu).

Xiyu Duan is with the Department of Biomedical Engineering, University of Michigan, Ann Arbor, MI 48104 USA (e-mail: dxy@umich.edu).

Mayur Birla and Kenn R. Oldham are with the Department of Mechanical Engineering, University of Michigan, Ann Arbor, MI 48104 USA (e-mail: mbirla@umich.edu; oldham@umich.edu).

Thomas D. Wang is with the Division of Gastroenterology, Department of Internal Medicine, University of Michigan, Ann Arbor, MI 48104 USA, also with the Department of Biomedical Engineering, University of Michigan, Ann Arbor, MI 48104 USA, and also with the Department of Mechanical Engineering, University of Michigan, Ann Arbor, MI 48104 USA (e-mail: thomaswa@umich.edu).

This article has supplementary downloadable material available at [ieeexplore.ieee.org](http://ieeexplore.ieee.org), provided by the authors.

Color versions of one or more of the figures in this article are available online at <http://ieeexplore.ieee.org>.

Digital Object Identifier 10.1109/TMI.2020.2971476

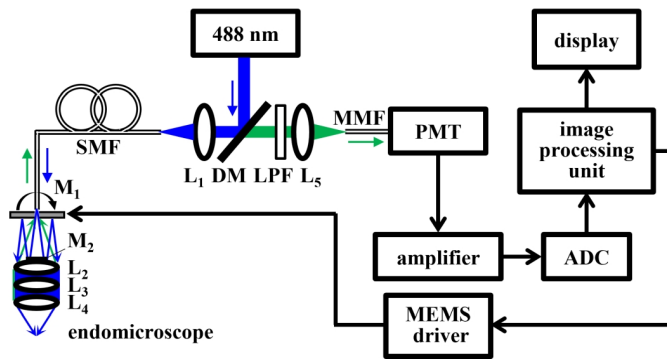


**Fig. 1.** Schematic of confocal imaging system. Details are provided in text. Key: ADC-- analog to digital converter, DM -- dichroic mirror,  $L_1$ - $L_5$ -- lenses, LPF-- long pass filter,  $M_1$  -- scan mirror,  $M_2$ -- fixed mirror, MMF -- multi-mode fiber, PMT -- photomultiplier, SMF -- single mode fiber.

have been demonstrated in endoscope prototypes with a variety of form factors [13]–[16]. All of these instruments have dimensions that are too large to pass forward through the standard working channel found in medical endoscopes. Micromachining techniques can also be used to fabricate precision apparatus to accurately align optics for efficient packaging. We aim to demonstrate a fiber-coupled, microsystems-based confocal endoscope with a rigid distal tip having sufficiently small dimensions to pass forward easily through a 2.8 mm diameter working channel. Instruments that can achieve this benchmark are compatible with a broad range of medical endoscopes frequently used in clinical practice.

## II. METHODS

### A. Imaging System

The schematic for the imaging system is shown, **Fig. 1**. A solid-state diode laser (OBIS 488 LS, Coherent) is used to deliver excitation at  $\lambda_{ex} = 488$  nm. The beam is deflected at  $90^\circ$  by a dichroic mirror (DM, Di02-R488-25 $\times$ 36, Semrock), and is focused by lens  $L_1$  (355151-A, Thorlabs) into a 4 meter long single mode optical fiber (SMF, S405-XP, Thorlabs) with  $3.3 \mu\text{m}$  mode field diameter and numerical aperture (NA) = 0.12 using FC/APC connectors. The beam exits the SMF, passes through the central aperture of scan mirror  $M_1$ , reflects off the fixed mirror  $M_2$ , and is scanned laterally by  $M_1$ . The beam is focused by the distal optics ( $L_2$ - $L_4$ ).

Fluorescence is collected by the same optics, passes through the DM and long pass filter (LPF, BLP01-488R-25, Semrock), is focused by lens  $L_5$  (355151-A, Thorlabs) into a 1 meter long multi-mode fiber (MMF, M31L01, Thorlabs) for delivery to a photomultiplier tube (PMT) detector (H7422-40, Hamamatsu). A high-speed amplifier (59-179, Edmund Optics) converts the current signal to a voltage. A multi-function data acquisition board digitizes the signal via an analog-to-digital converter (ADC, PCI-6115, National Instruments) at 10 M samples/sec. This board generates control signals via a digital-to-analog converter (DAC) that are sent to a high voltage amplifier (2350, Tegam) that drives the scan mirror  $M_1$ . Custom software (LabVIEW, National Instruments) is developed to deliver the drive signals, reconstruct the image, and perform data acquisition.

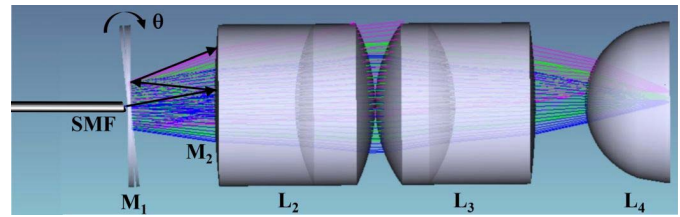


**Fig. 2.** Distal optics. The excitation beam is delivered via a SMF through the center aperture of mirror  $M_1$ . The path is folded on-axis to shorten the distal tip by reflecting the expanded beam between  $M_1$  and  $M_2$  prior to focusing by the optics ( $L_2$ - $L_4$ ).

### B. Optics Design

Ray-trace simulations were performed using ZEMAX (ver 13) optical design software to define parameters for the imaging optics. The design criteria included 1) diffraction-limited resolution on axis, 2) working distance (WD) =  $50 \mu\text{m}$ , and 3) a field-of-view (FOV) of  $350 \mu\text{m} \times 350 \mu\text{m}$ . Achromatic doublets are used for  $L_2$  and  $L_3$  to minimize spherical aberrations and chromatic dispersion, **Fig. 2**. A plano-convex lens with high refractive index is used for  $L_4$ . Only commercially available lenses with outer diameter (OD)  $\leq 2$  mm were considered for use in the prototype instrument. The optical path is folded to shorten the length of the distal tip and facilitate forward passage through the standard 2.8 mm diameter instrument channel found in many medical endoscopes. The input parameters used in the ZEMAX simulations are varied to choose the best optical elements for use in the prototype, and the final set is provided in the Results, A. Optics design. The complete technical specs for each element can be found from the part numbers and vendor websites.

### C. MEMS Scanner

A compact 2D electrostatic scanner was designed and fabricated using micro-electromechanical systems (MEMS) processes. The scanner operates based on the principle of parametric resonance whereby large mechanical scan angles can be achieved by driving the structure at  $2\omega_0/n$ , where  $\omega_0$  is the natural frequency of the structure and  $n$  is an integer [17]. The dimensions of the reflected beam incident on the surface of  $M_1$  defines the mirror geometry. The reflector is mounted on a gimbal that rotates about the X- and Y-axes, **Fig. 3a**.

A  $50 \mu\text{m}$  diameter central aperture was created to pass the excitation beam, **Fig. 3a**. This diameter allows for the beam to pass through unobstructed, and was determined from our ray-trace simulations using the numerical aperture of the fiber, distance between the fiber tip and top surface of MEMS chip, tilting angle, and alignment tolerance.

The frequency response is determined by a set of inner and outer multi-beam torsional springs coupled to comb-drive actuators designed to achieve resonance frequencies near 12 and 3 kHz for the fast and slow axes, respectively. The springs and actuators were designed using mixed stiffness-softening dynamics to generate large angular deflections [18]. The scanner was fabricated using a 3 step deep reactive-ion etch (DRIE) process using 3 masks, **Fig. 3b**.

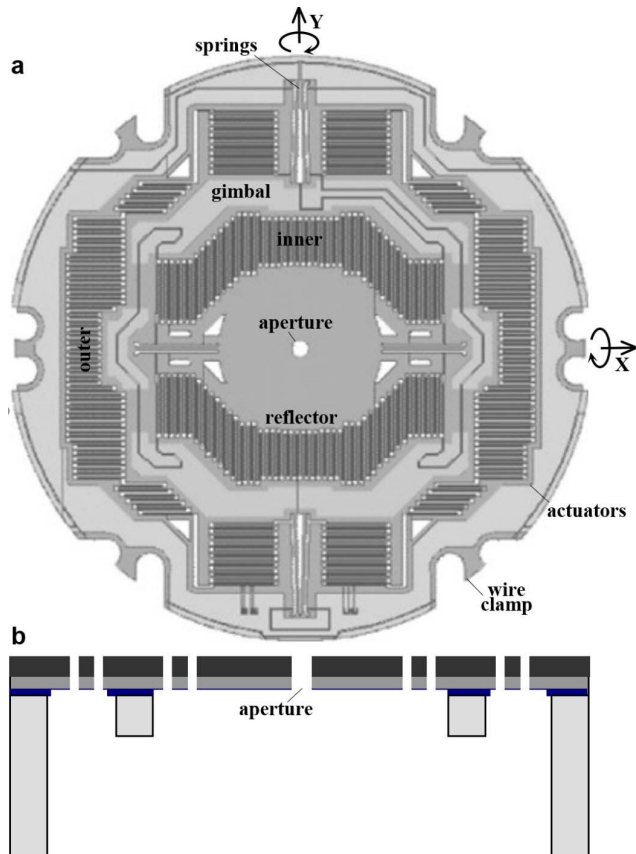


**Fig. 3.** MEMS scanner. (a) Scan mirror  $M_1$  is designed with a  $50\ \mu\text{m}$  diameter central aperture (front view) to pass the excitation beam. The reflector is mounted on an in-plane gimbal structure with separate inner and outer comb-drives actuators that deflect the reflector about the X- and Y- axes, respectively. This structure provides a large, stable Lissajous scan pattern without crosstalk. (b) A 3-step DRIE process is used to microfabricate the scanner (side view).

The thickness of the silicon layer is  $45\ \mu\text{m}$ . The scan mirror  $M_1$  creates images in a Lissajous pattern. Custom software (LabVIEW, National Instruments) was developed to drive the scanner and reconstruct the image by remapping the time series signal.

#### D. Scanner Packaging

A holder with 2 mm OD was designed to couple the SMF, mount the MEMS chip, and deliver the drive signals, Fig. 4. M3 crystal was used as the substrate for the holder. This acrylic based resin was chosen for its high strength and stiffness. This structure was fabricated using a 3D printer (ProJet 3500HD MAX, 3D Systems) with  $16\ \mu\text{m}$  resolution. The SMF was attached via a fiber ferrule.

The SMF was aligned with the center aperture in  $M_1$  using translational stages to make fine lateral adjustments. The SMF was axially translated to minimize the beam profile emerging from the distal optics. The distance between the scanner  $M_1$  and lens  $L_2$  was adjusted to achieve a  $\text{WD} = 50\ \mu\text{m}$ . The packaging arrangement for the SMF, ferrule, holder, and lenses ( $L_2$ - $L_4$ ) is shown, Fig. 5.

#### E. Image Reconstruction and Processing

The signal from the PMT was digitized at 10 M samples/sec. Confocal images were reconstructed in accordance with a

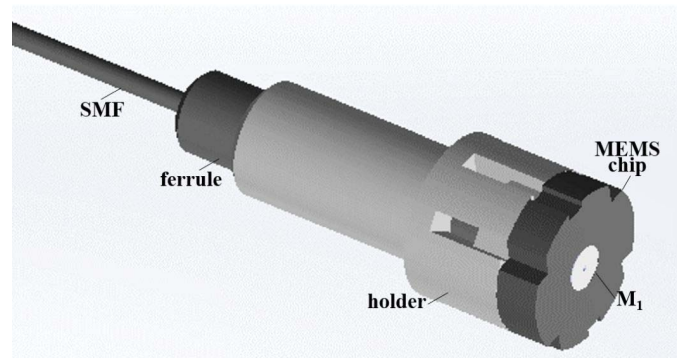


**Fig. 4.** MEMS holder. The structure used to couple the SMF to the MEMS chip and provide connectivity is shown.

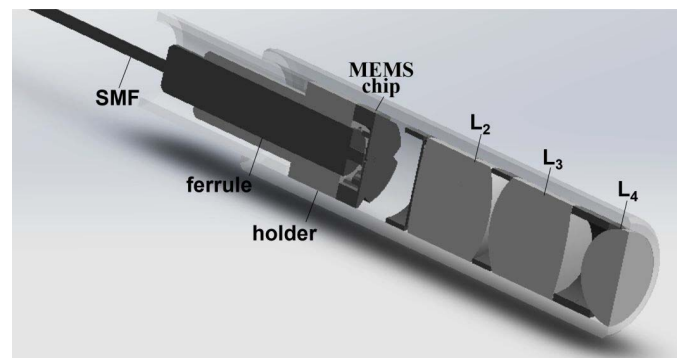


**Fig. 5.** Packaging scheme. Assembly of the SMF, holder, MEMS chip, and optics in the distal tip of the confocal endomicroscope is shown.

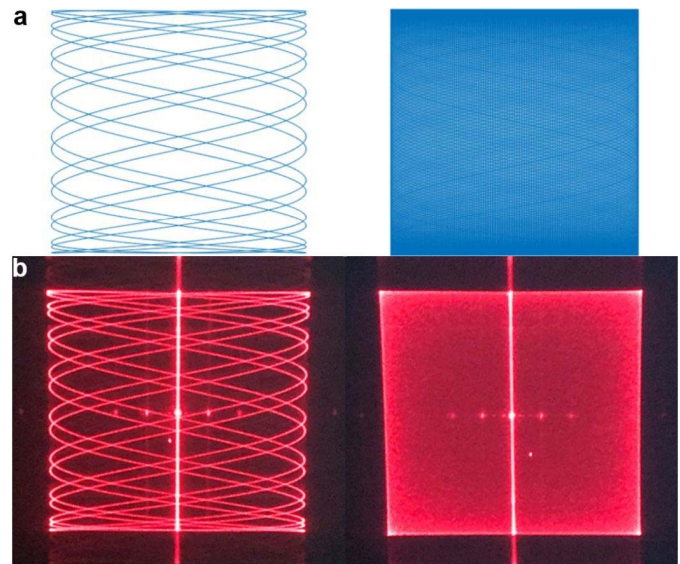


**Fig. 6.** Lissajous scan pattern. (a) Simulated trajectories with scan frequencies at  $f_x = 25.075\text{kHz}$  and  $f_y = 5.9\ \text{kHz}$  generate a sparse pattern (left), while  $f_x = 25.06\ \text{kHz}$  and  $f_y = 5.89\ \text{kHz}$  produce a dense pattern (right). (b) Experimental results with these parameters using  $\lambda = 635\ \text{nm}$  are shown.

Lissajous scan pattern [19], [20]. The time series of discrete data was mapped as intensities to each pixel location. The Lissajous trajectory was determined by the scan frequencies  $f_x$ ,  $f_y$ , and phase delays  $\phi_x$ ,  $\phi_y$  between the input drive voltage and the sinusoidal motion of the mirror in the X- and Y-axes, Fig. 6.

The pixel location  $(x, y)$  was mapped using the following equations:

$$x(t) = \frac{1}{2}P_x [\sin(2\pi f_x t + \varphi_x) + 1], \quad (1)$$

$$y(t) = \frac{1}{2}P_y [\sin(2\pi f_y t + \varphi_y) + 1], \quad (2)$$

where  $P_x$ ,  $P_y$  represent the image dimensions in terms of pixels.

The Lissajous scan patterns were sparse in the center of the image and increased in density towards the periphery. Unsourced pixels (empty spaces where beam is not scanned) were calculated by counting the number of pixels with intensity of zero. These unsourced pixels were filled in with the average intensities of eight neighboring pixels. This step was performed in real time during *in vivo* imaging. Dense scan regions resulted in assigning multiple intensity values to a pixel that are averaged to get the processed image.

The deflection amplitude and phase delay of the scan mirrors versus drive voltage were calibrated in the laboratory under ambient conditions prior to *in vivo* imaging. These parameters may drift over time after the instrument was inserted into the animal. The *in vivo* images can appear blurry due to perturbations in phase delay from environmental effects on the scan mirror dynamics, such as variations in temperature. These phase shifts can cause errors in assignment of intensity values to pixel locations. The actual phase delay of the scanner during *in vivo* use was recovered using a phase correction algorithm by optimizing a sharpness metric  $S$  defined by following equation:

$$S = \frac{1}{MN} \sum_i^M \sum_j^N (I(i, j) - I_{avg})^2, \quad (3)$$

where,  $I(i, j)$  are the gray scale intensities of the reconstructed image, and  $I_{avg}$  is the average of all the pixel intensities in the image.  $M$  and  $N$  are the total number of pixels along the height and width of the image. The phase corresponding to the sharpest image was selected as a new estimate for subsequent reconstruction of images and videos. Phase correction was performed either at regular time intervals or as needed. The resulting images were further processed using gamma correction to enhance image brightness and contrast. A Wiener filter was used to reduce shot and Gaussian noise from PMT and amplifier. This filter can suppress noise without blurring to minimize image degradation.

### F. In Vivo Images

Fluorescence images were collected *in vivo* from the epithelium in mouse colon *CPC;Apc* mice were genetically engineered to sporadically delete the *APC* gene, resulting in spontaneous formation of adenomas in the distal colon [21]. This model of colorectal cancer is representative of human disease as over 80% of all sporadic colorectal cancers have a mutation in *APC* [22]. This pre-clinical study was approved by the University Committee on the Use and Care of Animals (UCUCA) at the University of Michigan. During imaging, the mice were anesthetized with inhaled isoflurane. A small animal endoscope (27030BA, Karl Storz Veterinary Endoscopy) was used first to exam the colon for presence

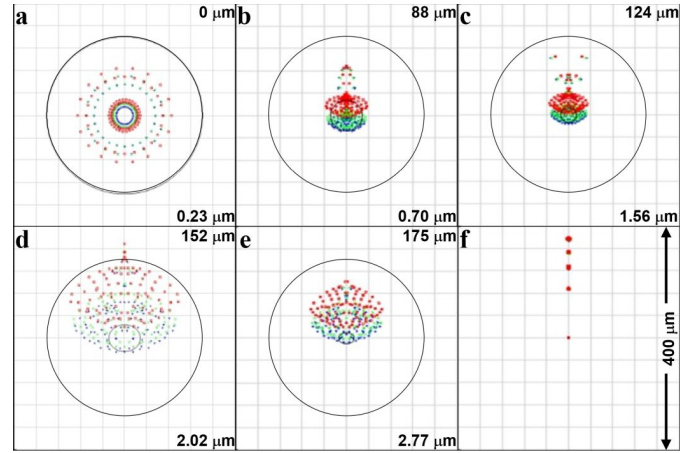


**Fig. 7.** Design of distal optics. (a-e) Model results show the focused beam achieves a spot size (defined by rms radius) of 0.23, 0.70, 1.56, 2.02, and 2.77  $\mu\text{m}$  at distances of 0, 88, 124, 152, and 175  $\mu\text{m}$  from the axis. (f) A FOV of 350  $\mu\text{m} \times 350 \mu\text{m}$  is obtained when  $M_1$  deflects at mechanical scan angles of  $\theta = \pm 8.25^\circ$ .

of adenomas. The approximate location of any found were identified, and the distance between the endoscope tip and the anus and the clockwise location of the adenoma were recorded for use as landmarks.

## III. RESULTS

### A. Optics Design

From the ray trace simulation results, achromats  $L_2$  (65568, Edmund Optics),  $L_3$  (65567, Edmund Optics), and plano convex lens  $L_4$  (90858, Edmund Optics) were identified as the best set of commercially available lenses with outer diameter  $\leq 2$  mm to use as focusing optics. An overall NA = 0.41 was achieved. This model predicts diffraction limited resolution on-axis and at lateral displacements up to 175  $\mu\text{m}$  from the image center, Fig. 7a-e. The chromatic focus shifts  $< 1.4 \mu\text{m}$  in the Z-axis from 480-600 nm.

A FOV of 350  $\mu\text{m} \times 350 \mu\text{m}$  is created when  $M_1$  deflects at mechanical scan angles of  $\theta = \pm 8.25^\circ$ , Fig. 7f. This panel shows 5 representative off-axis locations for the scanned beam to define the expected radius of the image field of view. The size of all beam spots is less than the Airy disk radius. Thus, the size of all beam spots is diffraction-limited rather than from spherical aberrations and beam degradation. The presence of the fixed mirror  $M_2$  results in a loss in power of 26.5% and 13% for the excitation and emission beams, respectively, in the center of the FOV and 25.5% and 12.5% at the image periphery.

### B. MEMS Scanner

The MEMS chip was fabricated with a circular geometry and 2 mm outer diameter (OD). The reflector is 550  $\mu\text{m}$  in width. The surface of  $M_2$  was coated with a  $\sim 70$  nm layer of aluminum to achieve  $> 90\%$  reflectivity between 400-700 nm [23]. A 50  $\mu\text{m}$  diameter aperture was etched in the center of the mirror to pass the excitation beam. Wire clamp structures were etched on the edges of the chip to reduce space used to deliver power and signal. The MEMS chip was secured onto a holder for alignment and packaging. A photo of the fabricated MEMS chip is shown, Fig. 8.

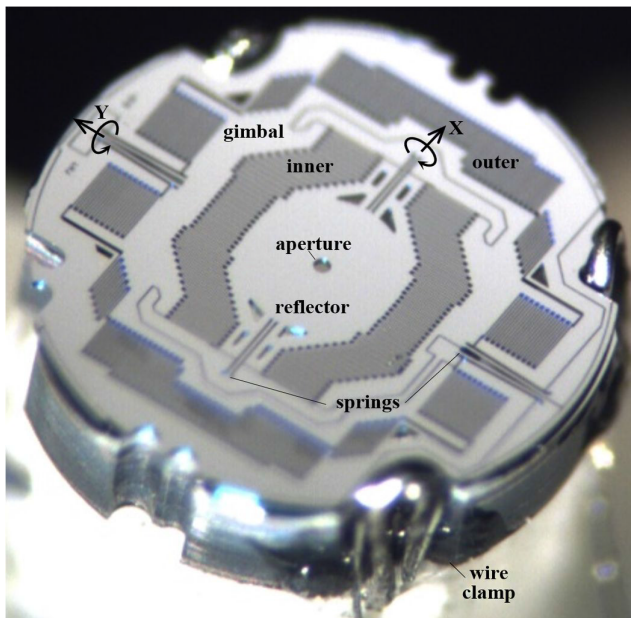


Fig. 8. MEMS chip. A photo is shown of the front surface of the microfabricated device.

TABLE I  
TRADE-OFFS IN IMAGE PARAMETERS

Image [pixels]	Frame rate [Hz]	Scan pattern density [%]
400×400	20	89.7
300×300	20	98.8
400×400	10	99.5
300×300	10	99.9

The image dimensions, frame rates, and scan pattern densities are shown using drive frequencies  $f_x = 27.68$  kHz and  $f_y = 6.54$  kHz with phase  $\varphi_x = 19.37^\circ$  and  $\varphi_y = 11.643^\circ$ . The pixel values were chosen to match the image field of view and resolution.

The mirror  $M_1$  achieves a large scan angle by sweeping the drive signal from high-to-low frequencies (downsweep) in either the X- or Y-axes, Fig. 9a, b. Sweeping in the opposite direction from low-to-high frequencies (upsweep) generates a smaller scan angle. The drive frequencies used were selected to generate a dense Lissajous scan pattern at high repetition rates. Sine waves with amplitudes of 60 V<sub>pp</sub> and frequencies near ~24 and ~6 kHz were used, and resulted in tilt frequencies of ~12 and ~3 kHz in the X- and Y-axes, respectively. A FOV of 350  $\mu\text{m} \times 350 \mu\text{m}$  was generated. This area was covered by maximum of 400  $\times$  400 pixels at a selectable frame rate, limited by image reconstruction computation time at a given frame rate, with a pixel spacing of 0.875  $\mu\text{m}$ . Motion artifact was reduced by imaging at higher speeds by using fewer pixels.

Tradeoffs among the number of pixels used to define the confocal image, frame rate, and scan pattern density are summarized, Table I. The scan pattern density is defined by the ratio of scanned area versus that of the total image.

$$\frac{\text{Total pixel size} - \text{Total zero intensity pixels size}}{\text{Total pixel size}} \times 100\%, \quad (4)$$

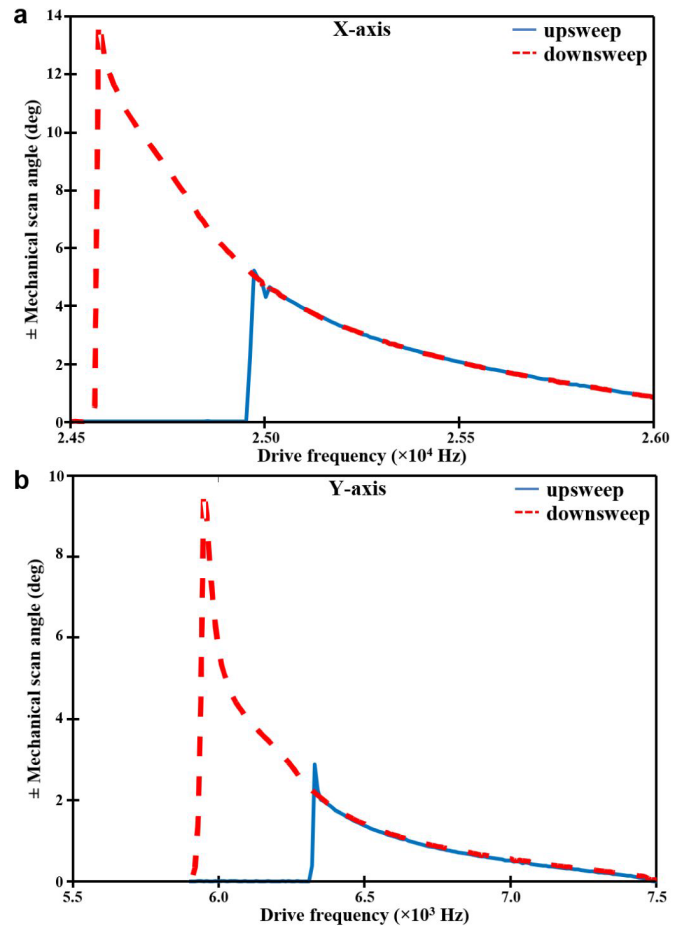


Fig. 9. Frequency response. Drive signals are delivered to mirror  $M_1$  with either an upsweep or downsweep in frequency. (a) In the X-axis, mechanical deflections  $>13^\circ$  can be achieved using a downsweep  $>2.45 \times 10^4$  Hz. (b) In the Y-axis, mechanical deflections  $>9^\circ$  can be achieved using a downsweep  $<6.0 \times 10^3$  Hz.

Increasing either the frame rate or pixel number will reduce the Lissajous scan density as result of a greater number of unsampled pixels.

### C. Scanner Packaging

The distal tip of the instrument was assembled within a stainless steel outer tube with 2.4 and 2.0 mm OD and ID, respectively, and 10 mm rigid length, Fig. 10a. The scanner was packaged in a sealed cavity to mitigate variations in ambient temperature and provide a stable environment. A 4 mm long stainless steel end tube with dimensions of 2.0 and 1.6 mm OD and ID, respectively, was inserted in between the rigid outer tube and the flexible tubing to isolate the scanner from unwanted mechanical vibrations.

Fine wires (B4421141, MWS Wire Industries) with 63  $\mu\text{m}$  OD thickness were attached directly to the clamps on the edge of the MEMS chip. Micromachining methods were used to fabricate the fixed mirror  $M_2$  and spacers used to mount the distal optics ( $L_2$ - $L_4$ ). The fixed mirror  $M_2$  was fabricated with a diameter of 0.29 mm to provide an adequate dimension to reflect the expanded excitation beam. For precise assembly of this tiny component, the fixed mirror was supported by a straight bar via a pair of flexible springs connected to

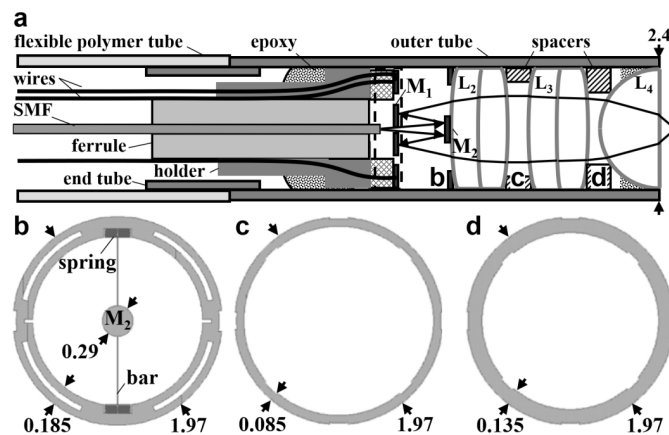


**Fig. 10.** Scanner packaging. (a) Schematic is shown for the assembly of the distal tip. (b) The fixed mirror  $M_2$  is supported by an  $8\ \mu\text{m}$  wide straight bar via a pair of flexible springs connected to the annular frame with dimensions of  $1.97$  and  $1.60\ \text{mm}$  OD and ID, respectively. The spacer between (c)  $L_2$  and  $L_3$  is  $1.97\ \text{mm}$  and  $1.80\ \text{mm}$  OD and ID, respectively, with a thickness of  $0.50\ \text{mm}$ , and that between (d)  $L_3$  and  $L_4$  has the same dimensions with a  $1.70\ \text{mm}$  ID.

the annular frame, Fig. 10b. Spacers were microfabricated to precisely position lenses  $L_2$ - $L_4$ , Fig. 10c, d.

Fixed mirror  $M_2$  and lens spacers were fabricated using micromachining techniques. Mirror  $M_2$  was formed on a  $40\ \mu\text{m}$  thick silicon device layer of an SOI wafer. Support was provided by a  $0.5\ \text{mm}$  thick SOI chip frame. A  $2\ \text{mm}$  diameter hole was opened below the mirror using link-arms to facilitate handling. The lens  $L_2$  was inserted into this hole and bonded to the fixed mirror  $M_2$  using UV glue. The SOI chip frame was then removed. Spacers were fabricated using a bulk-silicon-micromachining process to precisely position the individual components. The geometry and dimensions of these silicon parts were determined by the distance between the optics and the curvature and diameter of the lenses. The compact distal tip allows for easy forward passage through a standard  $2.8\ \text{mm}$  diameter working channel of a medical endoscope, Fig. 11a, b.

#### D. Image Resolution

The lateral and axial resolution of the instrument was characterized by a point spread function (PSF). Sub-resolution ( $100\ \text{nm}$  diameter) fluorescent beads (F-8803, Thermo Fisher Scientific) were imaged, and the full-width-at-half-maximum (FWHM) was determined. The axial response was measured by translating the beads in the vertical direction. The FWHM was found to be  $1.5$  and  $12\ \mu\text{m}$  in the lateral and axial dimensions, respectively, Fig. 12a, b. An image of a standard target verifies the lateral resolution measured by clearly distinguishing the set of bars in Group 7-6, Fig. 12c. A FOV of  $350\ \mu\text{m} \times 350\ \mu\text{m}$  is confirmed by the image of  $10\ \mu\text{m}$  diameter fluorescent beads (F-8836, Thermo Fisher Scientific) dispersed over a glass cover slip, Fig. 12d. In Fig. 12c, we adjusted the drive signal to slightly zoom in to better show the ability of the optics to distinguish the bars in Group 7-6. The field of view ( $275\ \mu\text{m} \times 275\ \mu\text{m}$ ) is only slightly smaller than that that used for in vivo imaging ( $350\ \mu\text{m} \times 350\ \mu\text{m}$ ).



**Fig. 11.** Confocal endomicroscope. (a) A photo is shown of the packaged flexible fiber instrument with distal tip dimensions of  $2.4\ \text{mm}$  diameter and  $10\ \text{mm}$  rigid length. (b) These ultra-compact dimensions allow for easy forward passage through the standard  $2.8\ \text{mm}$  diameter instrument channel of a medical endoscope (Olympus GIF-HQ190).

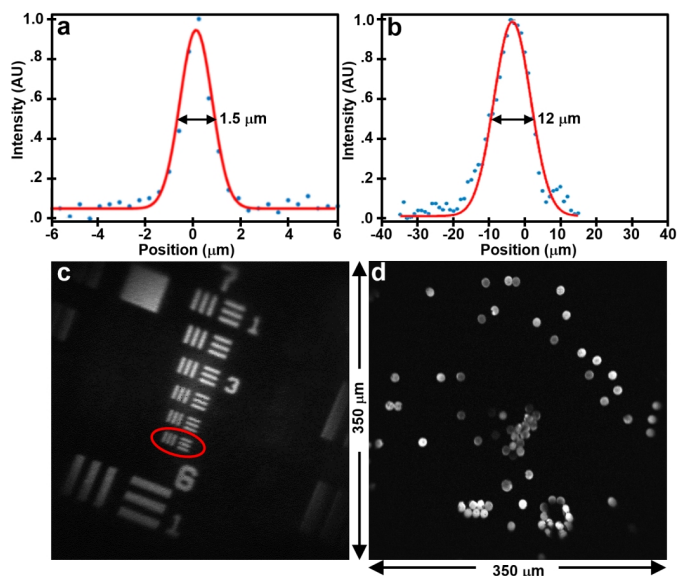


**Fig. 12.** Imaging performance. (a) A lateral and (b) axial resolution of  $1.5$  and  $12\ \mu\text{m}$ , respectively, was measured from the FWHM of sub-resolution fluorescent beads. (c) Group 7-6 (red oval) is distinguished on an image of a standard USAF-1951 bar target to verify lateral resolution measurement. (d) An image of dispersed fluorescent beads over a FOV of  $350\ \mu\text{m} \times 350\ \mu\text{m}$  is shown.

#### E. In Vivo Images

A FITC labeled peptide heterodimer specific for EGFR and ErbB2 was injected intravenously ( $12.5\ \text{mg/mL}$ ,  $100\ \mu\text{L}$ ) via tail vein [24]. The distal tip of the confocal endomicroscope was inserted into the colon and placed in contact with the adenomas using the defined landmarks as a guide. In vivo

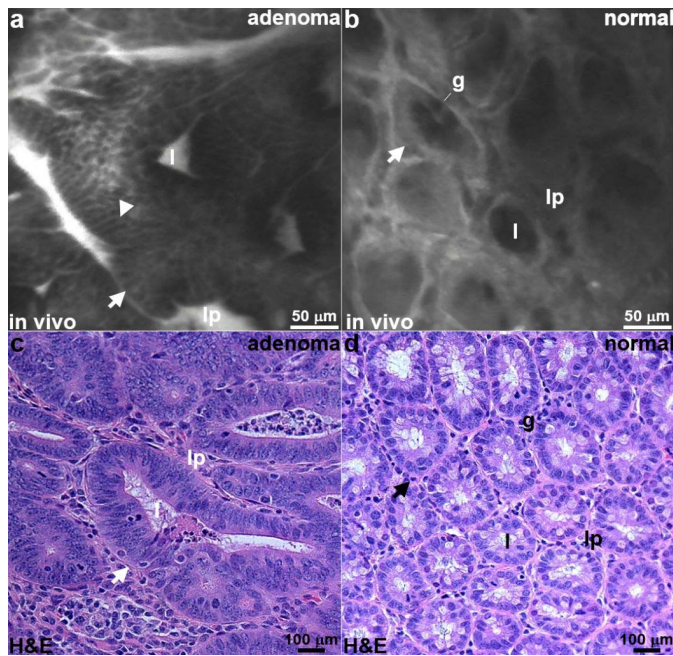


**Fig. 13.** In vivo confocal images. Fluorescence images are collected from an (a) adenoma and (b) normal mucosa in the colon of *CPC;Apc* mice following intravenous administration of a FITC-labeled peptide heterodimer to provide specific contrast. Strong staining is seen on the cell surface (arrowhead) in adenoma, and a non-specific pattern is seen for normal. Sub-cellular features, including crypt (arrow), lumen (l), goblet cell (g), and lamina propria (lp), can be seen. (c,d) Representative histology (H&E) for adenoma and normal is shown.

fluorescence images were collected at 10 frames per sec using 0.5 mW of laser power on the mucosal surface. From a representative confocal image of adenoma, the crypts (arrow) appeared irregular in shape and large in size, (video 1) Fig. 13a. A cell surface (arrowhead) staining pattern consistent with target expression was seen. In normal colonic epithelium, the crypts were circular in shape and have uniform dimensions, (video 2) Fig. 13b. The staining pattern was non-specific. Distinct crypt structures (arrow) can be identified, including the central lumen (l), goblet cells (g), and surrounding lamina propria (lp). Representative histology (H&E) is shown for adenoma and normal, Fig. 13c,d.

#### F. Ex Vivo Images

For ex vivo imaging, fluorescein sodium (FX0325, EMD Millipore) in solution (5% concentration, 200  $\mu$ L) was first administered intravenously via a tail vein injection. This contrast agent has been shown to be safe for human use [25]. The mice were euthanized, and the small bowel and kidney were excised for imaging. Fluorescence images of the small bowel show presence of villi (v) and lamina propria (lp), Fig. 14a. Confocal images from kidney show distinct renal tubules (t) and glomeruli (g), Fig. 14b. Representative histology (H&E) is shown for small bowel and kidney, Fig. 14c, d.

#### G. Image Reconstruction and Processing

The in vivo images were reconstructed using phase values that varied between  $\pm 5^\circ$  from the initial values. Without the phase correction, the Lissajous scan patterns can be misregistered and lead to duplicate pixels that blur the image,

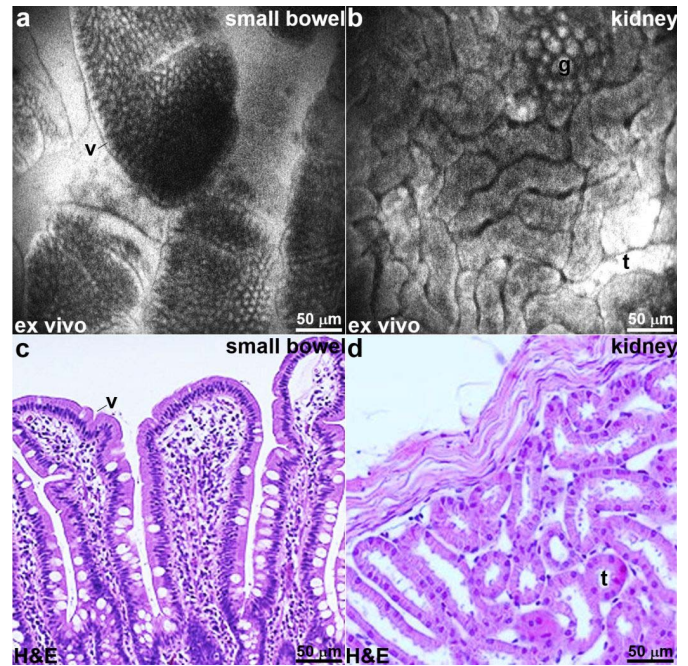


**Fig. 14.** Ex vivo confocal images. Fluorescence images are collected ex vivo from the (a) small bowel and (b) kidney following intravenous administration of fluorescein to provide non-specific contrast. Sub-cellular features, including villus (v), renal tubule (t), and glomerulus (g), can be visualized. (c,d) Representative histology (H&E) for small bowel and kidney is shown.

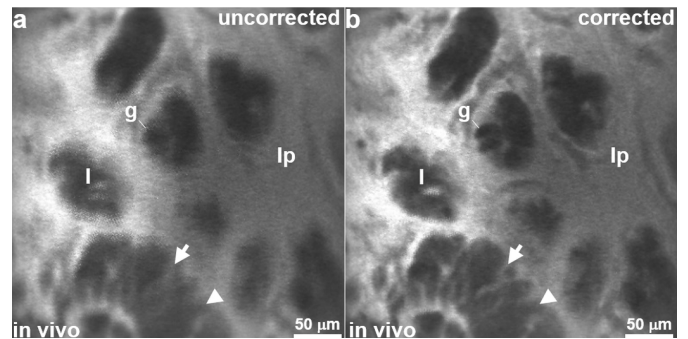


**Fig. 15.** Image processing. (a) Blurring results from misregistered pixels in an uncorrected confocal image collected in vivo from mouse colon. (b) After phase correction, sub-cellular features, including cell membrane (arrow) from an adenomatous crypt (arrowhead), and goblet cells (g) can be distinguished.

as shown by the unprocessed image of mouse colon collected in vivo, Fig. 15a. Typical phase shifts observed during the in vivo experiments were  $\sim 2-3^\circ$ . Correction resulted much sharper images whereby sub-cellular features could be distinguished, Fig. 15b. Environmental perturbations also affected signal amplitude, but these effects were small, and not addressed at this time. The phase shifts observed, and appeared to be caused by small fluctuations in temperature after the instrument was inserted into mouse colon. Corrections could be made without loss of image quality during in vivo imaging.

## IV. DISCUSSION

A prototype confocal endomicroscope has been demonstrated with distal tip dimensions of 2.4 mm diameter and 10 mm rigid length. To our knowledge, this is the first flexible fiber MEMS-based instrument that can pass forward

through a 2.8 mm diameter working channel found in standard medical endoscopes. Use of microsystems technology is a powerful approach to address the considerable challenges of limited space available to package the scanner and optics. Numerous designs have been reported, but none have realized sufficiently small dimensions to be used for real-time in-vivo imaging through a medical endoscope [26]–[29]. The length of the distal tip was reduced by folding the optical path on-axis while providing sufficient space for the beam to expand and achieve a high NA for sub-cellular resolution. Precision alignment apparatus were microfabricated to accurately position the optomechanical components inside the scanhead. Real-time fluorescence images were collected from mouse colon to demonstrate in vivo performance. Histology-like features were distinguished to identify pre-malignant from normal colonic mucosa. The ultra-compact dimensions of this instrument allow for broad clinical use by community physicians to perform “optical” biopsy.

An endomicroscope that uses a central aperture in the MEMS scanner to pass the incident beam has been previously reported [26]. This instrument was designed to collect reflectance images. A high level of light backscattered into the collecting fiber resulted in unacceptable noise that required an opening to be formed in the fixed mirror that reduced signal. The performance of the MEMS scanner was limited by mechanical and electrical crosstalk. A complex control circuit was required that increased complexity for image reconstruction. By comparison, our instrument was designed to collect fluorescence, and is not sensitive to back reflections. We use a parametric resonance mirror that produces large deflection angles to achieve a much larger field-of-view of  $350\ \mu\text{m} \times 350\ \mu\text{m}$  versus  $100\ \mu\text{m} \times 75\ \mu\text{m}$ . Our MEMS scanner employs an in-plane gimbal structure with separate comb-drives for actuation to create a stable Lissajous scan pattern to generate large deflection angles without crosstalk.

Microsystems technology was used to implement an efficient packaging strategy to scale down the dimensions of the distal tip. The MEMS chip was designed using clamp structures rather than bond pads to reduce the space needed to insert and connect wires to deliver power and signal. Conventional wire bonding methods require an additional substrate, such as a printed circuit board (PCB), to provide either through holes or pins. The space saved allows for use of a larger reflector to capture more light. Microfabrication techniques were also employed to produce spacers with high tolerance to precisely align the optics so that diffraction-limited resolution could be achieved using commercially-available optics. Large mechanical stresses are incurred on the distal tip when the instrument was passed through the working channel of the endoscope and when placed in direct contact with tissue. An end tube was used to support the interface between the flexible tubing and rigid housing and isolate the scanner from unwanted bending motions.

The scan mirror was designed based on the principle of parametric resonance to achieve large deflection angles in a device with a small footprint. The drive frequency was tuned

to near resonance in the response region to achieve a robust Lissajous scan pattern. Temperature variations from in vivo use can result in changes in phase, spring stiffness, and air damping effects. Small shifts in phase occurred when the instrument was inserted inside the mouse colon as a result of differences in core body versus room temperature. The confocal images were reconstructed using a pixel number and spacing determined by the expected FOV and lateral resolution. This ensures a Lissajous pattern with a high fill factor. A FOV of  $350\ \mu\text{m} \times 350\ \mu\text{m}$  was achieved using  $400 \times 400$  pixels with  $0.875\ \mu\text{m}$  pixel spacing. Images collected in vivo from the colon of anesthetized mice showed minimal motion artifacts. Table I shows the trade-offs in scan pattern density at higher frame rates. In addition to the subtraction algorithm, Eq. 3, we tried other conventional methods, including histogram and contrast limited adaptive histogram equalization, but these methods did not improve the quality of the images due to noise amplification and contrast degradation, respectively.

Our imaging system uses a point-detection PMT where a signal at the point of the Lissajous scan trajectory is mapped into a single pixel. Our imaging modality is different from that of a typical CCD or CMOS system where light is collected over entire field of view, and the signal is digitized and divided into pixels. This is where a Nyquist criterion is required to adequately reconstruct the analog signal. For a Lissajous scan-based imaging, the distance between each scan line determines the scan resolution which varies over scanning region. The scan patterns are sparse in the center of the image, where the scan speed is at its maximum, and becomes denser towards the periphery, Fig.6a. Hence, some parts of the image are oversampled while others are undersampled where the sampling rate is lower than the maximum scan speed or the scan trajectory does not provide full coverage of the region. The scan frequencies were thus carefully chosen to provide scan pattern density above 99%, Table I, without degrading image resolution, for the images and videos presented.

This 2.4 mm diameter design represents a major advance in scaling down the dimensions of MEMS endomicroscope technology. Previously, a 4.2 mm diameter side-view confocal instrument was demonstrated using a microactuator that performs axial translation [27]. The prototype could be inserted repetitively into mouse colon for in vivo imaging, but the distal tip was too wide to pass forward through the standard working channel of a medical endoscope. A 5.5 mm diameter confocal endomicroscope using the dual axes configuration has been developed [28]. Near-infrared fluorescence images in either the vertical or horizontal plane could be collected with either  $430\ \mu\text{m}$  depth or  $1\ \text{mm} \times 1\ \text{mm}$  area, respectively. This prototype could be inserted into rat colon for in vivo imaging. A 7 mm diameter confocal instrument using an electrothermal mirror that deflects at angles  $>26^\circ$  has been implemented [29]. A MEMS tunable microlens provides reflectance images with  $>400\ \mu\text{m}$  depth. A 2.5 mm diameter confocal endomicroscope based on piezo-driven fiber scanner has been developed [30]. This design combines the fiber scanner and a tunable lens to enable axial scan range of  $100\ \mu\text{m}$ .

Microsystems technology provides unmatched versatility to incorporate functionality in ultra-compact devices. Production costs are potentially much lower than that of competing approaches. The Cellvizio confocal endomicroscope (Mauna Kea Technologies) is designed using a coherent fiber optic bundle [31]. This bundle is expensive to manufacture, and the finite number of fibers and fiber core spacing limits the image field-of-view and resolution. The excitation beam is scanned at the proximal end using a large, bulky galvo. This method prevents important functions, such as axial scanning, to be performed. The Optiscan (Pentax Precision Instruments) confocal endoscope has a 5 mm diameter and 4 cm long rigid distal tip [32]. This design was integrated into a custom medical endoscope with an increased overall diameter. The large dimensions reduce the flexibility of the distal tip, and limits range for retroflexion. Images are collected at a slow rate of either 0.8 or 1.6 frames per second.

Our flexible fiber confocal instrument represents a major advance for *in vivo* imaging in the clinical setting. Microsystems technology is used to scale down the size of the scanning mechanism for efficient packaging in the distal tip. Imaging speeds up to 20 frames per second could be achieved. Although not demonstrated here, axial scanning capabilities can be incorporated to vary the working distance by using a 3-axis scanner that performs vertical displacements [27]. Passing the instrument forward rather than backwards through the working channel of the endoscope greatly increases clinical utility. An ultra-compact confocal endomicroscope has been demonstrated for broad compatibility with medical endoscopes used by community physicians to collect images *in vivo* and provide instant tissue pathology.

#### ACKNOWLEDGMENT

G. Li, X. Duan, M. Birla, T. D. Wang, and H. Li are inventors on patents filed by the University of Michigan on the technology presented. The authors would like to thank F. Wang for technical support.

#### REFERENCES

- [1] K. Maitland and T. D. Wang, "Endoscopy," in *Biomedical Technology and Devices Handbook*, 2nd ed. New York, NY, USA: Taylor & Francis, 2013, pp. 217–245.
- [2] C. Lahiff and J. E. East, "Endoscopic approach to polyp recognition," *Frontline Gastroenterol.*, vol. 8, no. 2, pp. 98–103, Apr. 2017.
- [3] D. Von Renteln and H. Pohl, "Polyp resection—controversial practices and unanswered questions," *Clin. Transl. Gastroenterol.*, vol. 8, no. 3, p. e76, Mar. 2017.
- [4] A. Lombardini *et al.*, "High-resolution multimodal flexible coherent Raman endoscope," *Light, Sci. Appl.*, vol. 7, no. 1, p. 1–8, 2018.
- [5] F. Akhondi, Y. Qin, N. Peyghambarian, J. K. Barton, and K. Kieu, "Compact fiber-based multi-photon endoscope working at 1700 nm," *Biomed. Opt. Express*, vol. 9, no. 5, pp. 2326–2335, 2018.
- [6] J. M. Yang *et al.*, "Three-dimensional photoacoustic endoscopic imaging of the rabbit esophagus," *PLoS ONE*, vol. 10, no. 4, Apr. 2015, Art. no. e0120269.
- [7] S. S. Chauhan *et al.*, "Confocal laser endomicroscopy," *Gastrointestinal Endoscopy*, vol. 80, no. 6, pp. 928–938, Dec. 2014.
- [8] M. Wallace *et al.*, "Miami classification for probe-based confocal laser endomicroscopy," *Endoscopy*, vol. 43, no. 10, pp. 882–891, Oct. 2011.
- [9] H. Neumann, R. Kiesslich, M. B. Wallace, and M. F. Neurath, "Confocal laser endomicroscopy: Technical advances and clinical applications," *Gastroenterology*, vol. 139, no. 2, pp. 388–392.e2, Aug. 2010.
- [10] D. L. Polla *et al.*, "Microdevices in medicine," *Ann. Rev. Biomed. Eng.*, vol. 2, no. 1, pp. 551–576, 2000.
- [11] L. Lin and E. Keeler, "Progress of MEMS scanning micromirrors for optical bio-imaging," *Micromachines*, vol. 6, no. 11, pp. 1675–1689, Nov. 2015.
- [12] S. A. Tadigadapa and N. Najafi, "Developments in microelectromechanical systems (MEMS): A manufacturing perspective," *J. Manuf. Sci. Eng.*, vol. 125, no. 4, pp. 816–823, Nov. 2003.
- [13] D. Lee, U. Krishnamoorthy, K. Yu, and O. Solgaard, "Single-crystalline silicon micromirrors actuated by self-aligned vertical electrostatic combdrives with piston-motion and rotation capability," *Sens. Actuators A, Phys.*, vol. 114, nos. 2–3, pp. 423–428, Sep. 2004.
- [14] J. Choi, T. Wang, and K. Oldham, "Dynamics of thin-film piezoelectric microactuators with large vertical stroke subject to multi-axis coupling and fabrication asymmetries," *J. Micromech. Microeng.*, vol. 28, no. 1, Jan. 2018, Art. no. 015014.
- [15] Q. Tanguy *et al.*, "Design and fabrication of a 2-axis electrothermal MEMS micro-scanner for optical coherence tomography," *Micromachines*, vol. 8, no. 5, p. 146, May 2017.
- [16] H. Mansoor, H. Zeng, K. Chen, Y. Yu, J. Zhao, and M. Chiao, "Vertical optical sectioning using a magnetically driven confocal microscanner aimed for *in vivo* clinical imaging," *Opt. Express*, vol. 19, no. 25, pp. 25161–25172, Dec. 2011.
- [17] K. L. Turner, S. A. Miller, P. G. Hartwell, N. C. Macdonald, S. H. Strogatz, and S. G. Adams, "Five parametric resonances in a microelectromechanical system," *Nature*, vol. 396, no. 6707, pp. 149–152, Nov. 1998.
- [18] H. Li *et al.*, "Integrated monolithic 3D MEMS scanner for switchable real time vertical/horizontal cross-sectional imaging," *Opt. Express*, vol. 24, no. 3, pp. 2145–2155, Feb. 2016.
- [19] C. L. Hoy, N. J. Durr, and A. Ben-Yakar, "Fast-updating and nonrepeating Lissajous image reconstruction method for capturing increased dynamic information," *Appl. Opt.*, vol. 50, no. 16, pp. 2376–2382, Jun. 2011.
- [20] M. Eli, "Jules Lissajous and his figures," in *Trigonometric Delight*. Princeton, NJ, USA: Princeton Univ. Press, 2013, ch. 11, pp. 145–149.
- [21] T. Hinoi *et al.*, "Mouse model of colonic adenoma-carcinoma progression based on somatic Apc inactivation," *Cancer Res.*, vol. 67, no. 20, pp. 9721–9730, Oct. 2007.
- [22] A. J. Rowan *et al.*, "APC mutations in sporadic colorectal tumors: A mutational 'hotspot' and interdependence of the 'two hits,'" *Proc. Nat. Acad. Sci. USA*, vol. 97, pp. 3352–3357, 2000.
- [23] A. D. Rakić, "Algorithm for the determination of intrinsic optical constants of metal films: Application to aluminum," *Appl. Opt.*, vol. 34, no. 22, pp. 4755–4767, Aug. 1995.
- [24] J. Chen *et al.*, "Multiplexed targeting of Barrett's neoplasia with a heterobivalent ligand: Imaging study on mouse xenograft *in vivo* and human specimens *ex vivo*," *J. Med. Chem.*, vol. 61, no. 12, pp. 5323–5331, Jun. 2018.
- [25] M. B. Wallace *et al.*, "The safety of intravenous fluorescein for confocal laser endomicroscopy in the gastrointestinal tract," *Alimentary Pharmacol. Therapeutics*, vol. 31, no. 5, pp. 548–552, Mar. 2010.
- [26] K. Murakami *et al.*, "A miniature confocal optical microscope with MEMS gimbal scanner," in *Proc. 12th Int. Conf. Solid-State Sens., Actuators Microsyst. (TRANSDUCERS)*, 2003, pp. 587–590.
- [27] X. Duan, H. Li, F. Wang, X. Li, K. R. Oldham, and T. D. Wang, "Three-dimensional side-view endomicroscope for tracking individual cells *in vivo*," *Biomed. Opt. Express*, vol. 8, no. 12, pp. 5533–5545, Dec. 2017.
- [28] G. Li *et al.*, "Visualizing epithelial expression in vertical and horizontal planes with dual axes confocal endomicroscope using compact distal scanner," *IEEE Trans. Med. Imag.*, vol. 36, no. 7, pp. 1482–1490, Jul. 2017.
- [29] L. Liu, E. Wang, X. Zhang, W. Liang, X. Li, and H. Xie, "MEMS-based 3D confocal scanning microendoscope using MEMS scanners for both lateral and axial scan," *Sens. Actuators A, Phys.*, vol. 215, pp. 89–95, Aug. 2014.
- [30] N. Weber, T. Meinert, H. Zappe, and A. Seifert, "Tunable MEMS fiber scanner for confocal microscopy," in *Proc. IEEE 27th Int. Conf. Micro Electro Mech. Syst. (MEMS)*, Jan. 2014, pp. 881–884.
- [31] E. Laemmel, M. Genet, G. Le Goualher, A. Perchant, J. F. Le Gargasson, and E. Vicaut, "Fibered confocal fluorescence microscopy (Cell-viZio) facilitates extended imaging in the field of microcirculation," *J. Vascular Res.*, vol. 41, no. 5, pp. 400–411, 2004.
- [32] R. Kiesslich *et al.*, "Confocal laser endomicroscopy for diagnosing intraepithelial neoplasias and colorectal cancer *in vivo*," *Gastroenterology*, vol. 127, no. 3, pp. 706–713, Sep. 2004.